

NLO QCD effects on angular observables in $e^-p \rightarrow e^-(\nu_e)Hj$ in presence of non-standard HVV couplings

Biswajit Das,^a Pramod Sharma^b and Ambresh Shivaji^b

^a*The Institute of Mathematical Sciences, IV Cross Road, Taramani, Chennai 600113, India*

^b*Department of Physical Sciences, Indian Institute of Science Education and Research Mohali, Knowledge city, Sector 81, Manauli, PO, Sahibzada Ajit Singh Nagar, Punjab, India, 140306*

E-mail: biswajitd@imsc.res.in, ph19010@iisermohali.ac.in,
ashivaji@iisermohali.ac.in

ABSTRACT: The single Higgs production in neutral-current (NC) and charged-current (CC) processes at an electron-proton (ep) collider is a useful channel to probe new physics effects in the Higgs coupling to vector boson (HVV). In this context, observables sensitive to non-standard couplings previously studied at leading order require improved theoretical precision through the inclusion of radiative corrections. In this work, we present a fully differential Higgs plus one jet production at next-to-leading-order (NLO) accuracy in QCD for both the NC and CC processes. For the proposed Large Hadron electron Collider (LHeC) configuration, with a 60 GeV electron beam and a 7 TeV proton beam, the total cross sections receive modest corrections with significantly reduced scale uncertainties. We find that in several kinematic distributions which are relevant to the analysis of HVV couplings, the NLO K-factors are not flat. Within the Standard Model, the polar angle of the electron (for NC) and the azimuthal angular correlation (for both NC and CC processes) receive maximum corrections in the range of 3-4% in certain bins. We also compute NLO QCD corrections in the presence of non-standard HVV interactions. The corrections in the azimuthal angular correlations are similar to the standard model predictions. For the polar angle of the electron, the corrections are sensitive to the nature of the HVV coupling.

Contents

1	Introduction	2
2	The Process	3
3	Calculations	4
4	IR singularities and Dipole subtraction	5
5	Checks	8
6	Numerical Results	8
6.1	SM prediction	9
6.2	New physics results	15
7	Conclusions	17

1 Introduction

Following the discovery of the Higgs boson (H) at the LHC [1, 2], various Higgs production channels have been studied to determine its couplings to other particles in the Standard Model (SM). Precise measurements of the Higgs couplings to electroweak gauge bosons (HVV) are crucial in order to test the mechanism of electroweak symmetry breaking in the SM [3, 4]. For this reason, vector boson fusion (VBF)—the second most prominent channel for single Higgs production—remains a key focus in LHC searches [5, 6]. The combined measurements by the CMS [7] and ATLAS [8] collaborations have achieved precision levels below 10% for these couplings. Due to the cleaner environment with reduced QCD backgrounds and other advantages discussed in Refs. [9–11], the LHeC provides a complementary setting to the LHC. Thus, it can play a significant role in probing potential new physics directions in HVV coupling.

The new physics can be parametrized by the most general Lorentz structure of two rank tensors made of momenta of vector bosons. The expression for the HVV vertex is given by [12–17]:

$$\begin{aligned} \Gamma_{HVV}^{\mu\nu}(p_1, p_2) = & g_V m_V \kappa_V g^{\mu\nu} - \frac{g}{m_W} [\lambda_{1V}(p_1^\nu p_2^\mu - g^{\mu\nu} p_1 \cdot p_2) \\ & + \lambda_{2V}(p_1^\mu p_1^\nu + p_2^\mu p_2^\nu - g^{\mu\nu} p_1 \cdot p_1 - g^{\mu\nu} p_2 \cdot p_2) \\ & + \tilde{\lambda}_V \epsilon^{\mu\nu\alpha\beta} p_{1\alpha} p_{2\beta}]. \end{aligned} \quad (1.1)$$

Here, p_1 and p_2 are the momenta of the vector bosons. The BSM parameters κ_V and $\lambda_{1V,2V}$ are associated with CP-even couplings, while $\tilde{\lambda}_V$ is associated with CP-odd coupling. $\epsilon^{\mu\rho\alpha\beta}$ is Levi-Civita tensor of rank 4 defined with $\epsilon^{0123} = 1$ prescription.

The non-standard HVV couplings introduced in Eq. 1.1 can be probed using observables sensitive to the Lorentz structure of the coupling. Several studies exploring these observables have been carried out at both hadron [18–23] and lepton [24–26] colliders. In our previous studies [27–29], we investigated non-standard couplings by analyzing the sensitivity of angular observables in single Higgs production via VBF channel at the ep collider. These studies estimated constraints on the BSM coupling parameters using angular observables computed at leading order (LO) in perturbation theory. However, higher-order corrections are essential to achieve a more precise understanding of these observables and of other kinematic distributions employed in selection cuts. Such corrections are expected to impact the bounds on BSM parameters derived from LO analyses. Some results focusing on the impact of Next-to-leading order (NLO) QCD and electroweak corrections, within the SM framework, in NC and CC processes already exist in the literature [30–33].

The publicly available Monte Carlo packages [34, 35] do not allow automated computation of QCD corrections in processes at the ep collider in the presence of non-standard

couplings. In this study, we develop an in-house Monte Carlo code which incorporates $\mathcal{O}(\alpha_s)$ QCD corrections in the standard model as well as in the presence of non-standard HVV couplings for the NC and CC processes at the ep collider. Apart from revisiting the calculation for the inclusive cross sections, we investigate the impact of corrections on angular observables sensitive to non-standard HVV couplings.

2 The Process

We are interested in computing NLO QCD corrections to $H + 1$ jet production in e^-p collision [27]. At the leading order (LO), we are studying neutral current (NC) process $e^-p \rightarrow e^-Hj$ and charged current (CC) process $e^-p \rightarrow \nu_e H j$. In the leading order (LO), there is only one tree-level Feynman diagram associated with each process. As depicted in Fig. 1, diagram (a) is for the NC process and diagram (b) for the CC process. HZZ vertex appears for NC current, and HWW vertex appears for CC current process. We are interested to see the new physics effects in these HVV vertices.

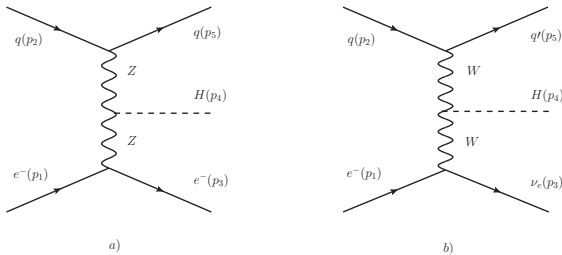


Figure 1: LO Feynman diagrams for NC and CC.

From Fig. 1, we see that there is one hadronic current and one leptonic current associated with tree-level diagrams. For this process, there is only one next-to-leading order diagram related to QCD vertex correction to the $qq'V$ vertex. The one-loop diagram is depicted in Fig. 2. For the inclusive observable, one also needs to consider the real emission diagrams. Gluons can be emitted from initial quarks as well as from final quarks. There are also gluon-initiated processes, where a gluon can split into one quark pair and one of them will participate in hard scattering. The inclusive processes are $e^-p \rightarrow e^-Hjj$ for NC and $e^-p \rightarrow \nu_e Hjj$ for CC process. There are two sub-processes corresponding to each real emission process. The two sub-processes are quark-initiated and gluon-initiated processes. There are two real emission diagrams corresponding to each sub-process as shown in Fig. 3. We have shown real emission diagrams only for the NC process, similar types of diagrams are there for the CC process.

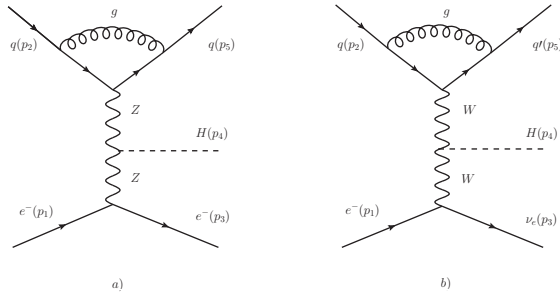


Figure 2: Virtual diagrams for NC and CC.

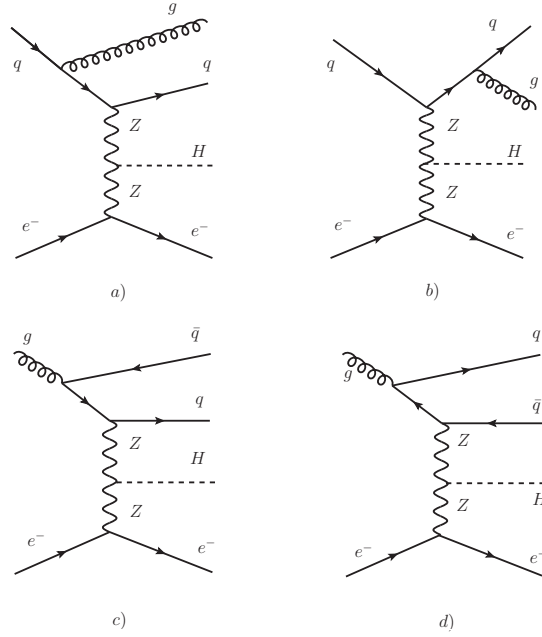


Figure 3: Real emission diagrams for NC.

3 Calculations

We calculate the helicity amplitudes for born, virtual, and real emission diagrams. As mentioned in the Sec. 2, there are one born, one one-loop, and four real emission (total) diagrams for each process (NC or CC). We take electron and light quarks as massless. The fermionic spinors have two helicity states, i.e, there can be 16 helicity amplitudes for born and virtual diagrams. Because of the vector current structure, only 4 of them will survive. In a similar fashion for real emission diagrams, out of 32 amplitudes, only 8 will survive. We use spinor helicity formalism to compute the helicity amplitudes [36]. This formalism is being done for massless fermions. We calculate the helicity amplitudes in terms of scalar spinor products $\langle pq \rangle$ or $[pq]$ [36, 37]. For real emission diagrams, there are gluons in the final

states. The polarization of gluons has to be contracted with tensor currents at the vertex, such as with $\langle p\gamma^\mu q \rangle$. We also compute the tensor currents from Dirac spinor solutions [38]. These currents follow all of the helicity identities in spinor helicity formalism. We compute helicity vectors' components numerically for massless gauge bosons.

We calculate the virtual diagrams in the HV dimensional scheme [39]. In this scheme, the loop part is being calculated in d -dimension and the rest is being calculated in 4-dimension. We get the analytical expression for the loop diagram in the HV scheme. It can be written as

$$\mathcal{M}^V = -\frac{\alpha_s(\mu_R)}{2\pi} \frac{(4\pi)^\epsilon}{\Gamma(1-\epsilon)} C_F \left(\frac{\mu^2}{2p_2 \cdot p_5} \right)^\epsilon \left\{ -\frac{1}{\epsilon^2} - \frac{3}{2\epsilon} - 4 + \mathcal{O}(\epsilon) \right\} \times \mathcal{M}^B. \quad (3.1)$$

Here, $\mathcal{M}^V, \mathcal{M}^B$ stand for virtual- and born-level amplitudes. $\mu(\mu_R)$ is the scale (renormalization scale) and $\alpha_s(\mu_R)$ is the strong coupling at μ_R . C_F is the color factor which is $\frac{4}{3}$. p_2 and p_5 are the momenta of the initial and final quarks, respectively. The pole ϵ is defined as $(4-d)/2$. As we see in Eq. 3.1, the virtual diagram has the highest pole $\frac{1}{\epsilon^2}$, which means the virtual diagram exhibits both soft and collinear divergences. We know that the weak coupling α_w does not get any quantum correction at one-loop QCD correction, and wave function renormalization vanishes in on-shell renormalization for massless fermions. Here, we do not need any renormalization and the $\frac{1}{\epsilon}$ pole in Eq. 3.1 is solely IR pole. The source of IR divergences and their cancellation with real emission diagrams have been discussed in Sec. 4 in great detail.

Once IR poles are removed from the renormalized amplitudes square, one has to perform the phase-space (PS) integrals for final state particles. Along with this, one has to perform an integral over the parton-distribution function (PDF) for each momentum fraction. As in e^-p collision, one proton is taking part in the collision, there will be one PDF to integrate. For the born and virtual diagrams, there are three body final state phase-space integrals, and for the real emission diagrams, there are four body final state phase-space integrals. We use RAMBOO [40] routine for phase-space points generators with given incoming momenta. The PDF and PS integral has been performed with the help of the Monte-Carlo integrator AMCI [41], which is based on VEGAS algorithm [42]. AMCI uses Parallel Virtual Machine PVM [43] for parallel computation across the physical CPUs. We generate all of our necessary distributions with the help of the AMCI. The subtlety of getting distributions regarding dipole subtraction has been discussed in the following section.

4 IR singularities and Dipole subtraction

The virtual diagrams in Fig. 2 are IR divergent. As one can see from the figure, three massless particles are meeting at a vertex, and two on-shell particles are exchanging one

massless particle, so the virtual diagrams are soft as well as collinear divergent [44]. The IR divergent structure we can see from Eq. 3.1. The poles in this equation are completely IR in nature. The real emission diagrams are also IR singular in soft and collinear regions due to the extra fermionic propagator, which splits into gluon and fermion. One can also show that real emission diagrams can exhibit the same pole structure as Eq. 3.1 if the phase-space for extra emission is integrated over in $d = 4 - 2\epsilon$ dimensions. Due to the collider search in fiducial regions and the complicated structure of the matrix element, we integrate the phase space over the emitted parton numerically. Also, we are interested in several kinematical distributions, which motivate us to develop a Monte-Carlo event generator for LO and NLO contributions.

We adopt Catany-Seymour dipole subtraction [45] to remove IR singularities from the inclusive partonic cross-section and to study inclusive differential distributions. The idea is to introduce a local counter-term which will absorb singularity from virtual amplitudes and at the same time exhibit point-wise singularities as the real emission amplitudes. The total inclusive cross-section can be written as

$$\sigma^{\text{NLO}} = \int_{m+1} d\sigma^{\text{R}} + \int_m d\sigma^{\text{V}} \quad (4.1)$$

Following the Ref. [45], we rewrite this Eq. as

$$\sigma^{\text{NLO}} = \int_{m+1} d\sigma^{\text{R}} - \int_{m+1} d\sigma^{\text{A}} + \int_m d\sigma^{\text{V}} + \int_{m+1} d\sigma^{\text{A}}. \quad (4.2)$$

The local counterterm $\delta\sigma^{\text{A}}$ has the same pointwise singular behavior as real emission diagrams in soft and collinear regions. Integrating over extra phase-space in $\delta\sigma^{\text{A}}$ will remove all of the IR singularities from virtual diagrams. We can write

$$\sigma^{\text{NLO}} = \int_{m+1} [d\sigma^{\text{R}} - d\sigma^{\text{A}}] + \int_m [d\sigma^{\text{V}} + \int_1 d\sigma^{\text{A}}]. \quad (4.3)$$

The last term in the second integral in the above equation will lead to the insertion operator \mathbf{I} which has to be convoluted with born level cross section. In this process, there is one identified parton in the initial state, and there is a finite remainder which is left after the factorization of initial state collinear singularities into the non-perturbative parton distribution functions (PDF). These terms are called \mathbf{P} , \mathbf{K} terms. Following the Ref. [45], we write the final dipole-subtracted NLO cross section as

$$\begin{aligned} \sigma^{\text{NLO}}(p) = & \int_{m+1} \left[(d\sigma^{\text{R}}(p))_{\epsilon=0} - \left(\sum_{\text{dipoles}} d\sigma^{\text{B}}(p) \otimes (dV_{\text{dipoles}} + dV'_{\text{dipoles}}) \right)_{\epsilon=0} \right] \quad (4.4) \\ & + \int_m [d\sigma^{\text{V}}(p) + d\sigma^{\text{B}}(p) \otimes \mathbf{I}]_{\epsilon=0} + \int_0^1 dx \int_m [d\sigma^{\text{B}}(xp) \otimes (\mathbf{P} + \mathbf{K})]_{\epsilon=0}. \end{aligned}$$

Where p is the momentum of the identified parton and x is the longitudinal fraction of p .

The initial and final state partons are quarks for these processes. The insertion operator \mathbf{I} which has been computed in d -dimensions, can be written as

$$\mathbf{I}(\epsilon) = \frac{\alpha(\mu_R)}{2\pi} \frac{(4\pi)^\epsilon}{\Gamma(1-\epsilon)} 2C_F \left(\frac{\mu}{2p_2 \cdot p_5} \right)^\epsilon \left\{ \frac{1}{\epsilon^2} + \frac{3}{2\epsilon} - \frac{\pi^2}{2} + 5 + \mathcal{O}(\epsilon) \right\} \quad (4.5)$$

For the processes under consideration, there is one initial state parton and one final state parton. So, only two dipole terms are needed. The dipole \mathcal{D}_{ij}^a is for when the final state parton is the emitter and the initial state is the spectator, and the dipole \mathcal{D}_k^{ai} is for when the initial state is the emitter and the final state is the spectator. These two dipoles, along with the real emission amplitude square, will project all singular numbers to regular numbers in singular regions.

The finite collinear remainder is

$$\sigma^{\text{NLO,c}}(\mu_R, \mu_F) = \sum_a \int_0^1 dx_a f_q^c(x_a, \mu_R^2, \mu_F^2) \hat{\sigma}_q^{\text{LO}}(x_a P, p_e; \{p_f\}) \quad (4.6)$$

where we define $f_q^c(x, \mu_F, \mu_R)$ as

$$f_q^c(x, \mu_F, \mu_R) = \frac{\alpha_s(\mu_R)}{2\pi} \left[\int_x^1 \frac{dz}{z} \left\{ f_g(x/z, \mu_F^2) A(z) + f_q(x/z, \mu_F^2) B(z) \right. \right. \quad (4.7) \\ \left. \left. + z f_q(x) C(z) \right\} + f_q(x) D(x) \right].$$

Following Ref. [45], we compute the integral kernels A, B, C, and D. They can be written as

$$A(z) = T_R \left\{ \left(z^2 + (1-z)^2 \right) \left(\ln \frac{1-z}{z} - \ln \frac{\mu_F^2}{2p_2 \cdot p_5} \right) + 2z(1-z) \right\} \quad (4.8)$$

$$B(z) = C_F \left\{ \frac{2\ln(1-z)}{1-z} - 2 \frac{\ln z}{1-z} - (1-z) \ln \frac{1-z}{z} + (1-z) \right. \quad (4.9) \\ \left. - \frac{3}{2} \frac{1}{1-z} - \frac{1+z^2}{1-z} \ln \frac{\mu_F^2}{2p_2 \cdot p_5} \right\}$$

$$C(z) = C_F \left\{ - \frac{2\ln(1-z)}{1-z} + \frac{3}{2} \frac{1}{1-z} + \frac{2}{1-z} \ln \frac{\mu_F^2}{2p_2 \cdot p_5} \right\} \quad (4.10)$$

$$D(x) = C_F \left\{ \ln^2(1-x) - \frac{\pi^2}{3} - 5 + \pi^2 - \frac{3}{2} \ln(1-x) - \frac{3}{2} \right. \quad (4.11) \\ \left. - \left(2\ln(1-x) + \frac{3}{2} \right) \ln \frac{\mu_F^2}{2p_2 \cdot p_5} \right\}$$

where $T_R = \frac{1}{2}$. These kernels have been consistent with the Ref. [31]

5 Checks

We check our calculations and implementation in several ways to avoid any subtle mistakes and ensure the reliability of our computations. Born level cross-sections for both NC and CC processes are in agreement with the `MadGraph` [35] results with the same set of SM parameters, PDF, and cuts. We have made the Ward identity check on the real amplitudes by replacing the polarization of the external gluon with its momentum. The real contribution is also in good agreement with the `MadGraph` with similar cuts on radiated partons. Virtual diagram calculation–pole structures, finite pieces match with the reference Ref. [31]. IR poles cancel with insertion operator \mathbf{I} . The dipole contribution approaches the real contribution in soft and collinear regions, making the net contribution (real-dipole) finite. This validates the correct implementation of the CS dipole subtraction scheme.

6 Numerical Results

We construct jets out of the final state partons to probe in fiducial regions and kinematical distributions. The tree level and virtual diagrams have only one parton in the final state, so there can be at most one jet production associated with the Higgs. This is the case with collinear remainder and dipole terms, as these contributions are convoluted with born contribution. The real emission diagrams have two partons in the final state, so there can be maximum two jets production associated with the Higgs. The jets are constructed from small-angle partons within the distance $R = 0.4$ in $(\eta - \phi)$ plane. We use `FastJet` [46, 47] package for jet clustering. We impose a minimum 20 GeV and 10 GeV cut on transverse momenta (p_T) of jets and electron (missing E_T for neutrinos), respectively. We also separate jets and electron but imposing a distance cut $\Delta R = 0.4$ in $(\eta - \phi)$ plane. The born, virtual, collinear kernels and dipoles are evaluated with three-body final state Monte-Carlo phase-space integration, whereas the real emission contribution has been evaluated with four-body final state Monte-Carlo phase-space integration. As the final state phase-space configurations are unequal for real emission and dipoles, they need to be computed separately. The kinematical cuts have to be implemented separately on real emissions and dipole contributions. The CS dipole subtraction ensures the cancellation of these two contributions in singular regions.

We use the SM parameters set from PDG2024 [48]. The masses and widths of vector bosons are taken as $M_W = 80.3692$ GeV, $M_Z = 91.188$ GeV, $\Gamma_W = 2.085$ GeV, and $\Gamma_Z = 2.4955$ GeV. The Higgs mass is taken as $M_H = 125$ GeV. We use $\alpha_W(M_Z) = 1/127.93$ in \overline{MS} scheme. We choose a dynamical scale choice for renormalization and factorization scale as

$$\mu_0 = \mu_R = \mu_F = \frac{1}{3} \left(p_{T;j} + \sqrt{M_H^2 + p_{T;H}^2} + p_{T;e^-/\nu_e} \right), \quad (6.1)$$

where p_T is the transverse momentum of the particle. We vary this scale in the range $0.5\mu_0 \geq \mu \geq 2\mu_0$ to measure the scale uncertainties. We use the LHAPDF [49] interface routine to calculate the strong coupling $\alpha_s(\mu_R)$ for each phase-space point. In the following, we define the *relative increment* at the level of total cross section due to NLO QCD correction as

$$\text{RI} = \frac{\sigma^{\text{NLO}} - \sigma^{\text{LO}}}{\sigma^{\text{LO}}} \times 100\% = (K - 1) \times 100\%.$$

In the above, $K = \sigma_{\text{NLO}}/\sigma_{\text{LO}}$ is defined as the NLO K-factor. We will use this quantity to discuss the QCD corrections in different bins of various kinematic and angular distributions.

6.1 SM prediction

First, we report NLO corrections to the total cross sections for the neutral current NC and CC processes, which are computed using the kinematic cuts outlined at the beginning of this section. In Tab. 1, we present LO and NLO cross sections using two PDF sets CT18 [50, 51] and NNPDF40 [52]. With the CT18 PDF, the SM cross-sections at LO and NLO for the NC process are 17.44 pb and 17.92 pb, respectively, while for the CC process they are 91.86 pb and 94.93 pb. We find positive NLO corrections, with the RI amounting to 2.72% for the NC process and 3.35% for the CC process. The CC process, therefore, exhibits a slightly larger correction compared to the NC process. In the table, the superscript and subscript to total cross-sections are scale uncertainties corresponding to $\mu = 0.5\mu_0$ and $\mu = 2\mu_0$, respectively. At LO, only the factorization scale μ_F enters through the PDF, while the renormalization scale μ_R appears at NLO through the strong coupling constant $\alpha_s(\mu_R)$. Therefore, the scale uncertainty at LO arises solely from variations in μ_F , and this is around $\pm 5\%$ for the NC and CC processes. At NLO, a partial cancellation of the μ_F dependence occurs between the PDF and the partonic cross section. Additionally, a relatively small size of the loop corrections results in a mild dependence on μ_R . Consequently, the overall scale uncertainty is reduced below 1% when going from LO to NLO. We also observe that the scale uncertainties are identical for both the NC and CC processes at each perturbative order. This is expected due to diagrammatic similarity between the two processes.

Process	PDF set	$\sigma^{\text{LO}}(\text{pb})$	$\sigma^{\text{NLO}}(\text{pb})$	RI(%)
NC	CT18	$17.44^{+5.27\%}_{-4.60\%}$	$17.92^{+0.04\%}_{-0.22\%}$	2.75
	NNPDF40	$19.57^{+4.82\%}_{-4.25\%}$	$18.23^{+0.18\%}_{-0.36\%}$	-6.85
CC	CT18	$91.86^{+5.29\%}_{-4.59\%}$	$94.93^{+0.06\%}_{-0.26\%}$	3.34
	NNPDF40	$100.89^{+4.74\%}_{-4.18\%}$	$95.69^{+0.30\%}_{-0.53\%}$	-5.15

Table 1: SM cross-sections and RIs due to NLO QCD corrections in the NC and CC processes for CT18 and NNPDF40 PDF sets. The numbers in the subscript and superscript denote the percentage scale uncertainties.

For NNPDF40 PDF set, the LO and NLO cross-sections are 19.57 (100.89) pb and 18.23 (95.69) pb for the NC (CC) process. On the contrary to the CT18 PDF choice, for the NNPDF40 PDF set, we get negative corrections with RI -6.85% and -5.15% in the NC and CC processes, respectively. Scale uncertainties at LO are similar to those for CT18 PDF. However, at NLO, these uncertainties are -0.36% (-0.53%) to +0.18% (+0.3%) for the NC(CC) process. Which indicates a bit larger scale uncertainty relative to CT18 PDF at NLO. The cross-section calculations for the choice of two different PDF sets can be used to estimate the PDF uncertainty. In this work, we present the rest of the results using CT18 PDF set only.

Now we discuss the effect of NLO corrections on the differential distributions essential for selection cuts to optimize the signal over background. In Fig. 4, we show the normalized transverse momentum (p_T) distributions, i.e., $\frac{1}{\sigma} \frac{d\sigma}{dp_T}$, for key final-state objects. These include the tagged jet and the Higgs boson in both the NC and CC processes. Additionally, we present the p_T distribution of the outgoing e^- in the NC channel and the missing transverse energy (\cancel{E}_T), arising from the neutrino, in the CC channel. We observe that the p_T distributions for each final state in both the NC and CC processes exhibit a similar pattern of NLO corrections. For the Higgs boson, the correction is -1% at low p_T and gradually rises with increasing p_T , reaching up to +5%. In case of the tagged jet, it receives corrections of up to +2.5% at low p_T , which become negative at higher p_T , reaching up to -1% in the tail of the distribution. In particular, the behavior of the NLO corrections in the p_T distribution for the jet closely follows the behavior reported in Ref. [31]. The NLO corrections to the p_T distribution of the e^- in the NC process and the missing transverse

energy (\cancel{E}_T) in the CC process increase progressively toward the high- p_T region. For the electron, the corrections reach up to approximately 10%, while for \cancel{E}_T , the corrections remain below 9%.

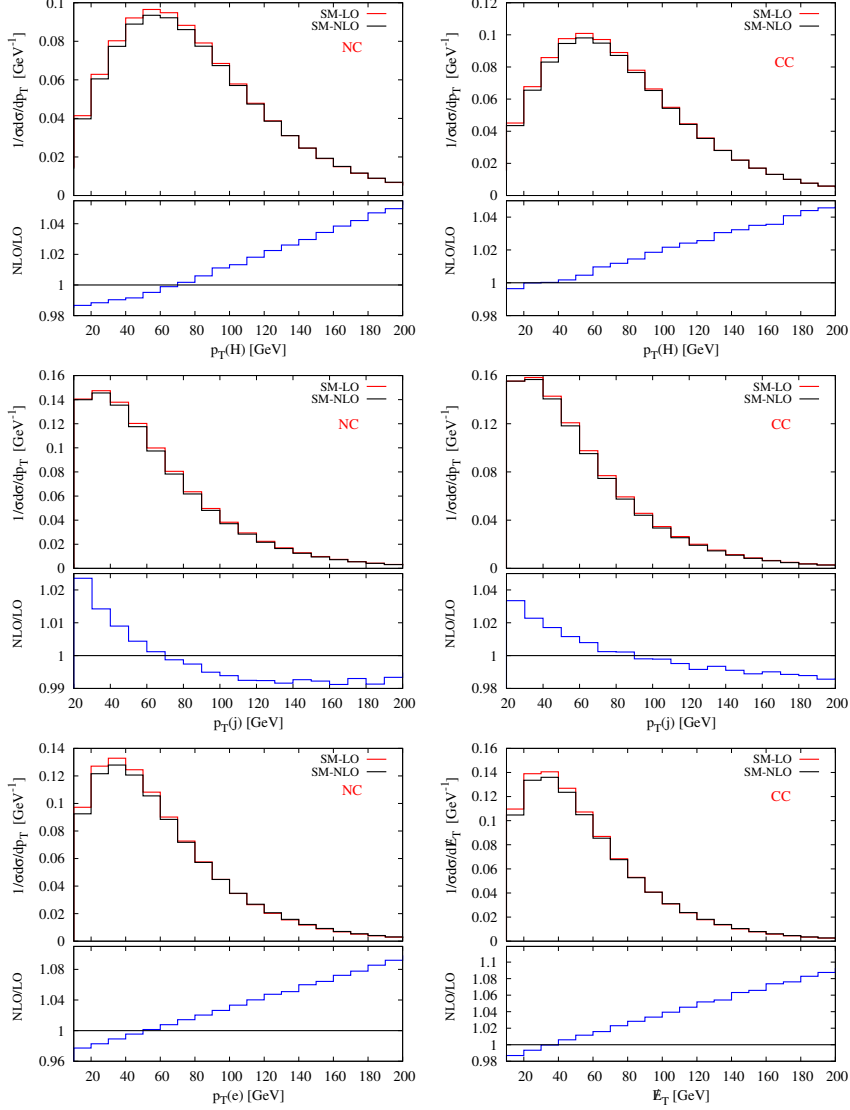


Figure 4: Upper panel: LO (red) and NLO QCD (black) predictions for p_T distribution of final state particles in the NC (left) and CC (right) processes with SM couplings. Lower panel: NLO K-factor (blue) in different bins of the p_T distributions.

The normalized pseudo-rapidity distributions ($\frac{1}{\sigma} \frac{d\sigma}{d\eta}$), along with the corresponding K-factors, for the final-state particles in the NC and CC processes are shown in Fig. 5. In both processes, the NLO corrections lead to a noticeable shift in the η distributions of the Higgs boson and the tagged jet toward higher rapidity. In the case of the tagged jet, this behavior

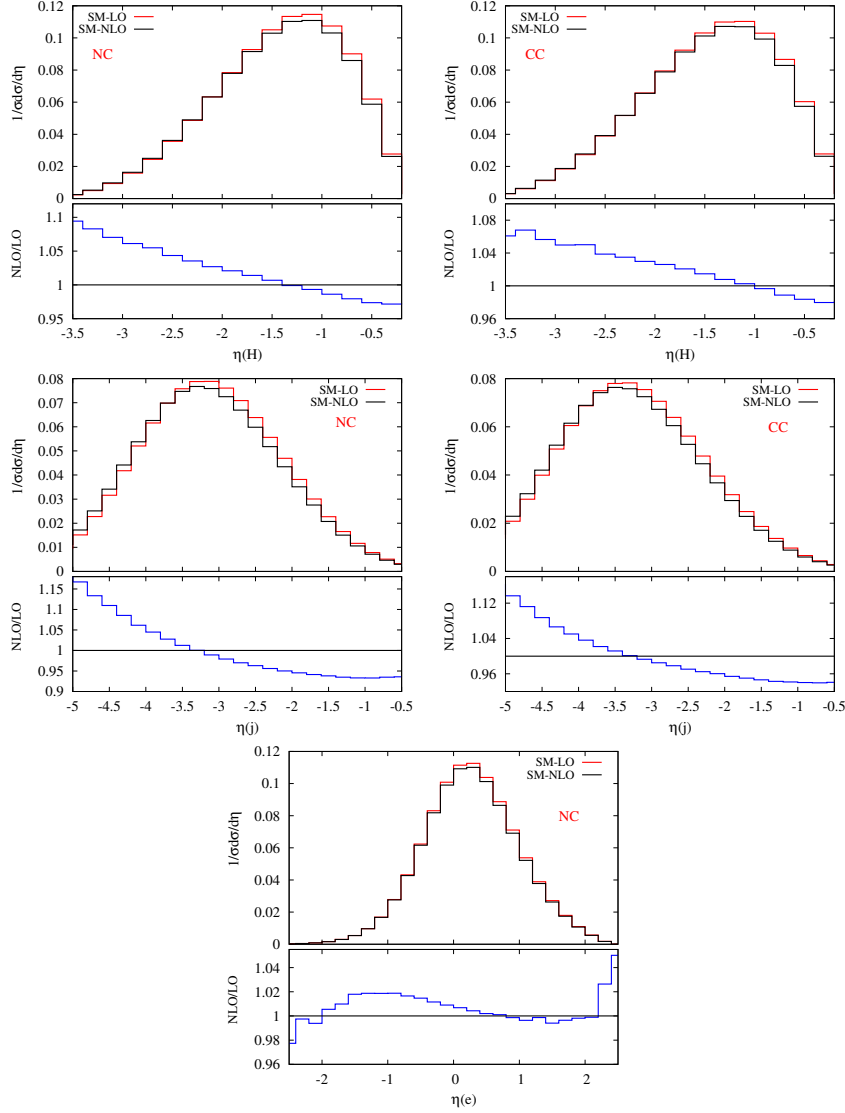


Figure 5: Upper panel: LO (red) and NLO QCD (black) predictions for pseudo-rapidities of observed final state particles in NC (left) and CC (right) processes with SM couplings. Lower panel: NLO K-factor (blue) in different bins of the η distributions.

can be attributed to the emission of an additional parton at NLO. The NLO corrections to the pseudo-rapidity distribution of the Higgs boson range from approximately -2.5% to +10% in the NC process and -2% to +7% in the CC process. However, the corrections for the tagged jet are larger, varying between -6% to 16% in the NC channel, and between -6% to 14% in the CC channel. The η distribution for the electron in the NC process experiences the correction ranging from -2% to 5%. The behavior of the NLO correction in the p_T distribution for the scattered e^- (and jet) and the η distribution for the jet is

consistent with the findings reported in Ref. [31].

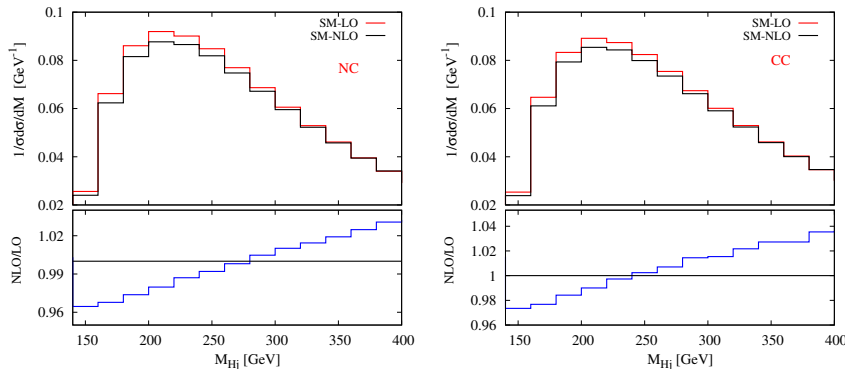


Figure 6: Upper panel: LO (red) and NLO QCD (black) predictions for the Higgs-jet invariant mass (M_{Hj}) distribution in the NC (left) and CC (right) processes with SM couplings. Lower panel: NLO K-factor (blue) in different bins of the M_{Hj} distributions.

The invariant mass distribution of the Higgs boson and the leading jet (M_{Hj}) plays a critical role in optimizing the signal-to-background ratio. Consequently, understanding the impact of QCD corrections on this distribution is essential. In Fig. 6, we present the impact of QCD corrections on the M_{Hj} distribution for both the NC and CC processes. In the NC process, the corrections start at approximately -4% for lower values of M_{Hj} , gradually increase with increasing M_{Hj} , and reach up to +3.5% in the high- M_{Hj} tail. In the CC process, a similar trend is observed, with corrections ranging from -2% to +4% across the bins.

The angular observables that provide the most stringent constraints on the HVV coupling are discussed in Ref. [27–29] in detail. In the NC process, these observables include θ_e , the polar angle of the scattered electron; α_{ej} , the angle between scattered e^- and the jet; β_{ejH} , the angle between Higgs and normal to the plane of e^- and jet; and $\Delta\phi_{ej}$, the azimuthal correlation of the electron and the jet, which ranges from $-\pi$ to π . In case of the CC process, $\Delta\phi_{\cancel{E}j}$ distributions are relevant for the discussion because information only in the transverse plane is accessible due to missing energy in this process. These observables have been studied at LO in perturbation theory and require higher-order corrections to capture their behavior more precisely, thereby potentially affecting the constraints on the HVV coupling parameters.

The θ_e , α_{ej} , and β_{ejH} distributions associated with the NC process are presented in Fig. 7. The θ_e and α_{ej} distributions are correlated, and consequently, their NLO corrections exhibit a similar pattern as well, reaching up to 5% in certain bins. The β_{ejH} is a CP-sensitive observable which is symmetric about $\pi/2$ [28]. Due to the CP-even nature of the

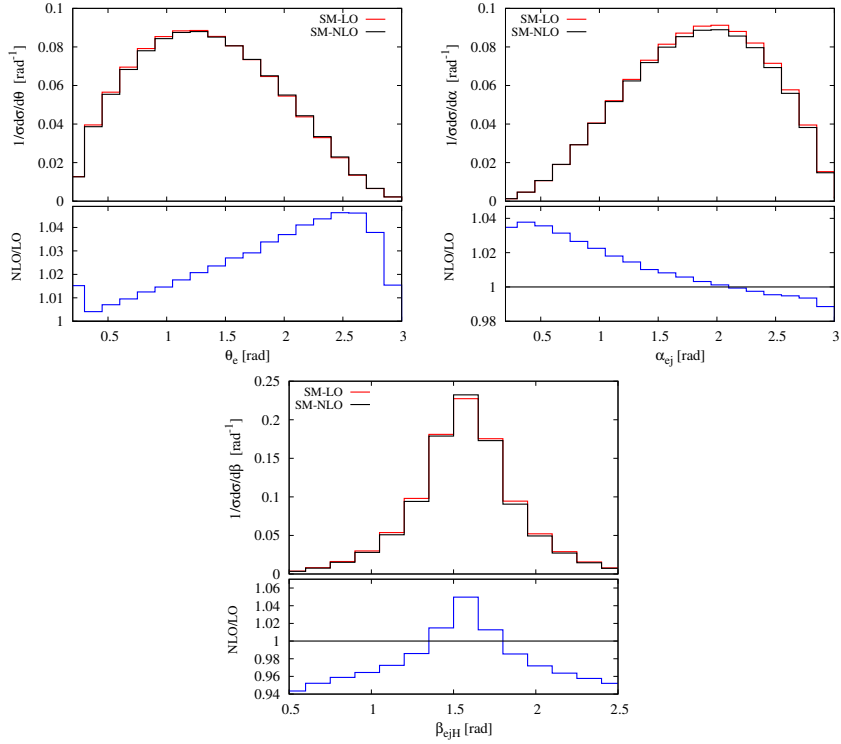


Figure 7: The LO (red) and NLO (black) predictions for angular variables θ_e , α_{ej} , and β_{ejH} for NC in SM. The bin-wise NLO K-factors are shown in the lower panels.

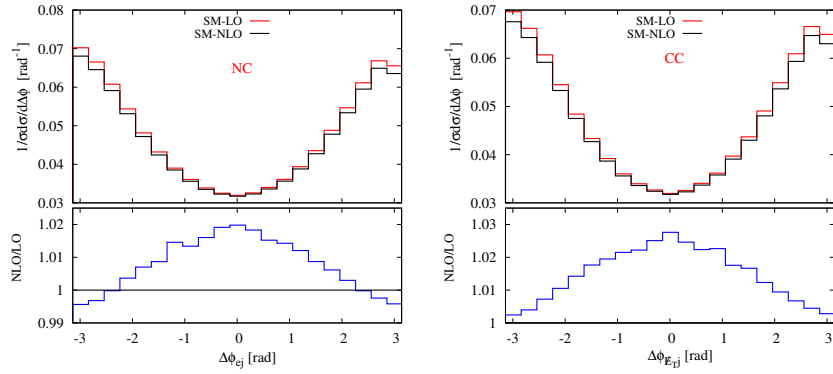


Figure 8: The LO (red) and NLO QCD (black) predictions for angular variables $\Delta\phi$, for NC (left) and CC (right) in SM. The bin-wise NLO K-factors are shown in the lower panels.

QCD interactions, the NLO corrections are also symmetric, with positive shifts reaching up to +5% in the central region and -6% in the outer bins. In Fig. 8, we present the $\Delta\phi_{ej}$ distribution for the NC process and the $\Delta\phi_{\cancel{e}j}$ distribution for the CC process. Similar to β_{ejH} , these observables display a symmetric correction pattern around the central bin. This is expected as β_{ejH} and $\Delta\phi_{ej}$ are correlated and differ mainly in normalization [28]. Notably, the NLO corrections to $\Delta\phi_{ej}$ and $\Delta\phi_{\cancel{e}j}$ are comparable in both magnitude and behavior. The corrections are around 2 – 3% in the mid region of both distributions.

6.2 New physics results

The NC and CC processes involving non-standard HVV couplings also receive NLO QCD corrections on the $qq'V$ vertex, similar to the purely SM scenario. We keep one BSM parameter associated with each component of HVV coupling non-zero at a time. We choose benchmark values for the HZZ parameters as $\lambda_{1Z} = 0.4$, $\lambda_{2Z} = 0.3$, and $\tilde{\lambda}_Z = 0.5$. For the HWW coupling, the benchmark values are $\lambda_{1W} = 0.07$, $\lambda_{2W} = 0.02$, and $\tilde{\lambda}_W = 0.2$. These values are motivated by constraints obtained from a cross-section level χ^2 analysis described in the Ref. [27].

Process		σ^{LO} (pb)	σ^{NLO} (pb)	RI(%)
NC	λ_{1Z}	$29.22^{+5.30\%}_{-4.60\%}$	$29.88^{+0.40\%}_{-0.40\%}$	2.26
	λ_{2Z}	$13.69^{+6.71\%}_{-5.70\%}$	$14.12^{+0.32\%}_{-0.63\%}$	3.14
	$\tilde{\lambda}_Z$	$25.25^{+5.46\%}_{-4.77\%}$	$25.92^{+0.46\%}_{-0.57\%}$	2.65
CC	λ_{1W}	$99.48^{+5.23\%}_{-4.55\%}$	$102.65^{+0.25\%}_{-0.36\%}$	3.19
	λ_{2W}	$82.20^{+5.25\%}_{-4.54\%}$	$84.86^{+0.25\%}_{-0.36\%}$	3.24
	$\tilde{\lambda}_W$	$102.39^{+5.32\%}_{-4.63\%}$	$105.71^{+0.35\%}_{-0.36\%}$	3.24

Table 2: Cross-sections with scale uncertainties and the corresponding RIs due to NLO QCD corrections for the NC and CC processes for benchmark values $(\lambda_{1Z}, \lambda_{2Z}, \tilde{\lambda}_Z) = (0.4, 0.3, 0.5)$ and $(\lambda_{1W}, \lambda_{2W}, \tilde{\lambda}_W) = (0.07, 0.02, 0.2)$.

In Tab. 2, we see that the cross-section for the NC process at NLO changes by 2.3% to 3.1% for all three BSM parameters of HZZ couplings relative to the LO contribution. Similarly, the cross-section for the CC process receives around 3.2% corrections for all three BSM parameters of HWW couplings relative to the LO contribution. These corrections are

consistent with the NLO corrections to the SM processes shown in Tab. 1. At LO, the scale uncertainty is around approximately $\pm 5\%$ for both the NC and CC processes, similar to their associated SM predictions. At NLO, uncertainties are around approximately $\pm 0.4\%$ for both the NC and CC processes.

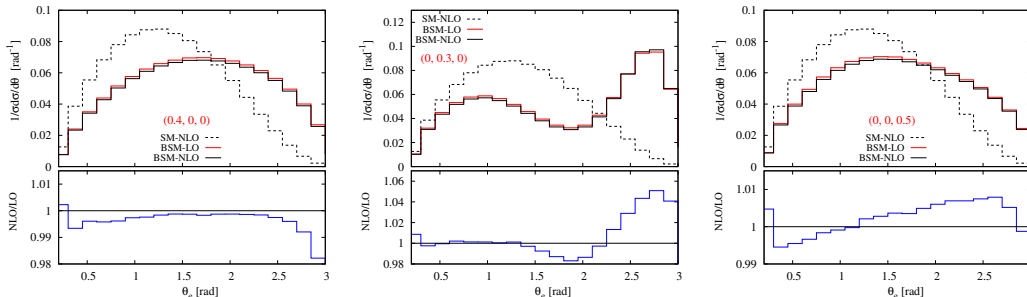


Figure 9: The LO (red) and NLO QCD (black) predictions for θ_e in NC process for benchmark values $\lambda_{1Z} = 0.4$, $\lambda_{2Z} = 0.3$ and $\tilde{\lambda}_Z = 0.5$ (left-to-right). For comparison, the SM results at NLO are also shown using dashed lines. The NLO K-factors (blue) are shown in the lower panels.

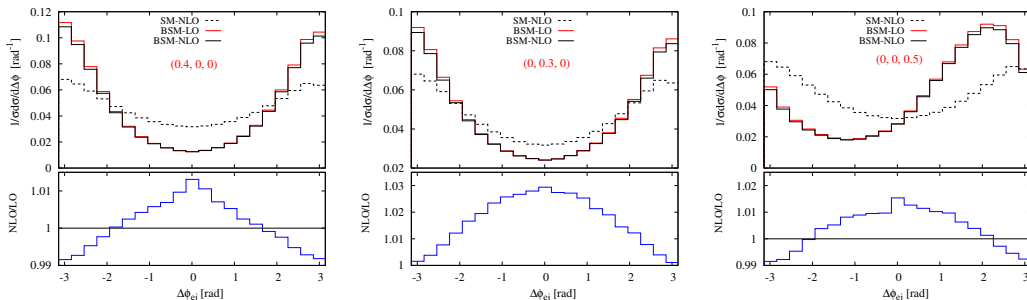


Figure 10: The LO (red) and NLO QCD (black) predictions for $\Delta\phi_{ej}$ in the NC process for benchmark values $\lambda_{1Z} = 0.4$, $\lambda_{2Z} = 0.3$ and $\tilde{\lambda}_Z = 0.5$ (left-to-right). For comparison, the SM results at NLO are also shown using dashed lines. The NLO K-factors (blue) are shown in the lower panel.

As discussed in Ref. [28], the observables θ_e and $\Delta\phi_{ej}$ exhibit the highest sensitivity to non-standard HZZ couplings, while $\Delta\phi_{\cancel{e}j}$ is most sensitive to deviations in the HWW coupling. We, therefore, restrict our discussions in this section to these angular observables only. In our previous study, we found that θ_e is best suited for constraining the λ_{2Z} parameter. As can be seen in Fig. 9, the presence of non-standard couplings shifts the θ_e distribution towards π with respect to the SM prediction. For λ_{1Z} and λ_{2Z} , the QCD corrections to θ_e range from -2% to 0.2% and -2% to 5% , respectively. In the case of $\tilde{\lambda}_Z$,

the corrections go from -0.5% to 1% across the bins.

The $\Delta\phi_{ej}$ distribution being CP-sensitive observable has been found suitable for efficiently constraining the $\tilde{\lambda}_Z$ parameter [28]. In Fig. 10, the QCD corrections in the presence of BSM parameters of the HZZ coupling in the NC process are shown. For the λ_{1Z} and λ_{2Z} , corrections are symmetric around the central bin. The corrections for λ_{1Z} are -1% in outer bins and go up to $+1.5\%$ in the mid region. In case of λ_{2Z} , the distribution has corrections as large as $+3\%$ in central bins. For $\tilde{\lambda}_Z$, the correction is -1% in outer bins, and $+1.5\%$ in the central region.

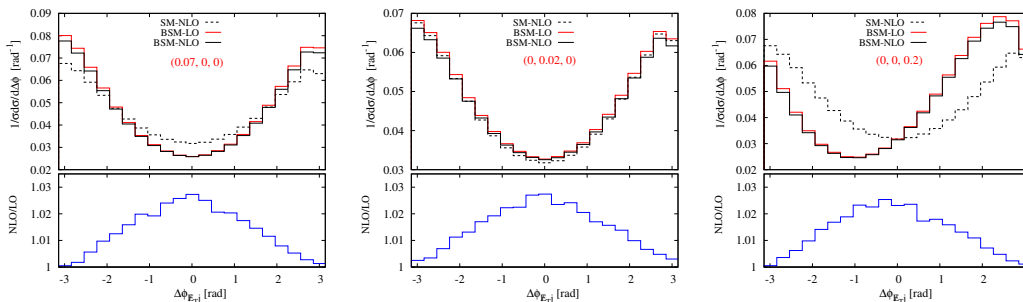


Figure 11: The LO (red) and NLO QCD (black) predictions for $\Delta\phi_{\cancel{e}j}$ in the CC process for benchmark values $\lambda_{1W} = 0.07$, $\lambda_{2W} = 0.02$ and $\tilde{\lambda}_W = 0.2$ (left-to-right). For comparison, the SM results at NLO are also shown using dashed lines. The NLO K-factors (blue) are shown in the lower panel.

For the CC process, due to the non-observability of the final state neutrino, the only angular observable of interest is $\Delta\phi_{\cancel{e}j}$, which is most sensitive to $\tilde{\lambda}_W$ parameter. The impact of QCD corrections on this observable is shown in Fig. 11 for the benchmark values of the non-standard HWW interaction parameters. For each BSM parameter associated with a similar Lorentz structure of HZZ and HWW coupling, the pattern of correction in the $\Delta\phi_{\cancel{e}j}$ distribution is similar to that of the $\Delta\phi_{ej}$ distribution. We observe that the $\Delta\phi_{\cancel{e}j}$ distributions receive about 2.5% corrections for λ_{1W} , and λ_{2W} , and $\tilde{\lambda}_W$.

7 Conclusions

In this work, we presented NLO QCD corrections to single Higgs production via the VBF process at ep collider with a 60 GeV electron beam and a 7 TeV proton beam. For the NC and CC processes with purely SM couplings, the NLO corrections enhance the total cross section by approximately 2.7% and 3.3%, respectively. We find that the corrections are highly PDF set dependent. A similar level of enhancement is observed when non-standard HVV couplings are included. The scale uncertainty, which is about $\pm 5\%$ at LO,

is significantly reduced to the permille level at NLO, which shows significant improvement in theoretical precision. We have also studied the K -factor bin by bin for each distribution, which gives us more insight into the nature of QCD corrections in different phase-space regions.

We also examined the impact of QCD corrections on key differential distributions relevant for event selection, such as the p_T , η , and invariant mass. Except for $\eta(j)$, all other kinematic observables receive modest corrections similar to the total cross section. The correction in the case of $\eta(j)$, however, can go beyond 10% in the high rapidity regions. Furthermore, we studied angular observables that are sensitive to non-standard HVV interactions, including θ_e , α_{ej} , β_{ejH} and $\Delta\phi_{ej}$ in the NC channel, and $\Delta\phi_{\cancel{E}j}$ in the CC channel. In both the standard model and in the presence of non-standard HVV couplings, the corrections for these distributions are small, but the K-factors change non-trivially across the bins.

Although the QCD corrections in the NC and CC are small, their precise impact on constraining the CP-even and CP-odd parameters of HVV couplings requires a systematic inclusion of QCD corrections in background processes as well. Now that electroweak corrections are also available and they affect kinematic distributions significantly, their inclusion in the signal-background analysis is also desirable.

Acknowledgements

BD would like to acknowledge Tousik Samui and Luca Buonocore for valuable discussions.

References

- [1] ATLAS collaboration, G. Aad et al., *Observation of a new particle in the search for the Standard Model Higgs boson with the ATLAS detector at the LHC*, *Phys. Lett. B* **716** (2012) 1 [[1207.7214](#)].
- [2] CMS collaboration, S. Chatrchyan et al., *Observation of a New Boson at a Mass of 125 GeV with the CMS Experiment at the LHC*, *Phys. Lett. B* **716** (2012) 30 [[1207.7235](#)].
- [3] P. W. Higgs, *Broken Symmetries and the Masses of Gauge Bosons*, *Phys. Rev. Lett.* **13** (1964) 508.
- [4] P. W. Higgs, *Broken symmetries, massless particles and gauge fields*, *Phys. Lett.* **12** (1964) 132.
- [5] M. Spira, *Higgs Boson Production and Decay at Hadron Colliders*, *Prog. Part. Nucl. Phys.* **95** (2017) 98 [[1612.07651](#)].
- [6] LHC HIGGS CROSS SECTION WORKING GROUP collaboration, D. de Florian et al., *Handbook of LHC Higgs Cross Sections: 4. Deciphering the Nature of the Higgs Sector*, *CERN Yellow Rep. Monogr.* **2** (2017) 1 [[1610.07922](#)].

- [7] CMS collaboration, A. Tumasyan et al., *A portrait of the Higgs boson by the CMS experiment ten years after the discovery.*, *Nature* **607** (2022) 60 [2207.00043].
- [8] ATLAS collaboration, G. Aad et al., *A detailed map of Higgs boson interactions by the ATLAS experiment ten years after the discovery*, *Nature* **607** (2022) 52 [2207.00092].
- [9] LHeC, FCC-HE STUDY GROUP collaboration, P. Agostini et al., *The Large Hadron–Electron Collider at the HL-LHC*, *J. Phys. G* **48** (2021) 110501 [2007.14491].
- [10] LHeC STUDY GROUP collaboration, J. L. Abelleira Fernandez et al., *A Large Hadron Electron Collider at CERN: Report on the Physics and Design Concepts for Machine and Detector*, *J. Phys. G* **39** (2012) 075001 [1206.2913].
- [11] F. Ahmadova et al., *The Large Hadron electron Collider as a bridge project for CERN*, 2503.17727.
- [12] M. L. Stong and K. Hagiwara, *Probing the scalar sector in $e^+ e^- \rightarrow f \text{ anti-} f \text{ phi}$* , in *2nd International Workshop on Physics and Experiments with Linear $e^+ e^-$ Colliders*, 8, 1993, hep-ph/9307255.
- [13] S. Dutta, K. Hagiwara and Y. Matsumoto, *Measuring the Higgs-Vector boson Couplings at Linear $e^+ e^-$ Collider*, *Phys. Rev. D* **78** (2008) 115016 [0808.0477].
- [14] S. S. Biswal, R. M. Godbole, B. Mellado and S. Raychaudhuri, *Azimuthal Angle Probe of Anomalous HWW Couplings at a High Energy ep Collider*, *Phys. Rev. Lett.* **109** (2012) 261801 [1203.6285].
- [15] A. Alloul, B. Fuks and V. Sanz, *Phenomenology of the Higgs Effective Lagrangian via FEYNRULES*, *JHEP* **04** (2014) 110 [1310.5150].
- [16] M. Kumar, X. Ruan, R. Islam, A. S. Cornell, M. Klein, U. Klein et al., *Probing anomalous couplings using di-Higgs production in electron–proton collisions*, *Phys. Lett. B* **764** (2017) 247 [1509.04016].
- [17] A. I. Hernández-Juárez, G. Tavares-Velasco and A. Fernández-Télez, *New evaluation of the HZZ coupling: Direct bounds on anomalous contributions and CP-violating effects via a new asymmetry*, *Phys. Rev. D* **107** (2023) 115031 [2301.13127].
- [18] T. Han and Y. Li, *Genuine CP-odd Observables at the LHC*, *Phys. Lett. B* **683** (2010) 278 [0911.2933].
- [19] N. D. Christensen, T. Han and Y. Li, *Testing CP Violation in ZZH Interactions at the LHC*, *Phys. Lett. B* **693** (2010) 28 [1005.5393].
- [20] S. Dwivedi, D. K. Ghosh, B. Mukhopadhyaya and A. Shivaji, *Distinguishing CP-odd couplings of the Higgs boson to weak boson pairs*, *Phys. Rev. D* **93** (2016) 115039 [1603.06195].
- [21] N. Desai, B. Mukhopadhyaya and D. K. Ghosh, *cp-violating hww couplings at the large hadron collider*, *Phys. Rev. D* **83** (2011) 113004.

- [22] T. Plehn, D. L. Rainwater and D. Zeppenfeld, *Determining the Structure of Higgs Couplings at the LHC*, *Phys. Rev. Lett.* **88** (2002) 051801 [[hep-ph/0105325](#)].
- [23] V. Hankele, G. Klamke, D. Zeppenfeld and T. Figy, *Anomalous Higgs boson couplings in vector boson fusion at the CERN LHC*, *Phys. Rev. D* **74** (2006) 095001 [[hep-ph/0609075](#)].
- [24] T. Han and J. Jiang, *CP violating $Z Z H$ coupling at $e^+ e^-$ linear colliders*, *Phys. Rev. D* **63** (2001) 096007 [[hep-ph/0011271](#)].
- [25] K. Hagiwara, S. Ishihara, J. Kamoshita and B. A. Kniehl, *Prospects of measuring general Higgs couplings at $e^+ e^-$ linear colliders*, *Eur. Phys. J. C* **14** (2000) 457 [[hep-ph/0002043](#)].
- [26] H.-D. Li, C.-D. Lü and L.-Y. Shan, *Sensitivity study of anomalous HZZ couplings at a future Higgs factory*, *Chin. Phys. C* **43** (2019) 103001 [[1901.10218](#)].
- [27] P. Sharma and A. Shivaji, *Probing non-standard HVV ($V = W, Z$) couplings in single Higgs production at future electron-proton collider*, *JHEP* **10** (2022) 108 [[2207.03862](#)].
- [28] P. Sharma and A. Shivaji, *Role of angular observables in probing non-standard HZZ couplings at an electron-proton collider*, [2506.02558](#).
- [29] P. Sharma, B. Das and A. Shivaji, *NLO QCD effects on angular observables in single Higgs production at electron-proton collider*, *PoS ICHEP2024* (2025) 085 [[2411.07950](#)].
- [30] J. Blumlein, G. J. van Oldenborgh and R. Ruckl, *QCD and QED corrections to Higgs boson production in charged current $e p$ scattering*, *Nucl. Phys. B* **395** (1993) 35 [[hep-ph/9209219](#)].
- [31] B. Jager, *Next-to-leading order QCD corrections to Higgs production at a future lepton-proton collider*, *Phys. Rev. D* **81** (2010) 054018 [[1001.3789](#)].
- [32] B. Wang, K. Wang and H. Xiong, *Electroweak corrections to Higgs boson production via $W W$ fusion at the future LHeC*, *Phys. Rev. D* **106** (2022) 093011 [[2207.14515](#)].
- [33] H. Xiong, H. Hou, Z. Qian, Q. Xu and B. Wang, *Electroweak corrections to Higgs boson production via $Z Z$ fusion at the future LHeC*, *Phys. Rev. D* **109** (2024) 116021 [[2311.14912](#)].
- [34] SHERPA collaboration, E. Bothmann et al., *Event generation with Sherpa 3*, *JHEP* **12** (2024) 156 [[2410.22148](#)].
- [35] J. Alwall, R. Frederix, S. Frixione, V. Hirschi, F. Maltoni, O. Mattelaer et al., *The automated computation of tree-level and next-to-leading order differential cross sections, and their matching to parton shower simulations*, *JHEP* **07** (2014) 079 [[1405.0301](#)].
- [36] M. E. Peskin, *Simplifying Multi-Jet QCD Computation*, in *13th Mexican School of Particles and Fields*, 1, 2011, [1101.2414](#).
- [37] R. Kleiss and W. Stirling, *Cross sections for the production of an arbitrary number of photons in electron-positron annihilation*, *Physics Letters B* **179** (1986) 159.
- [38] B. Das, *Probing Anomalous Higgs Boson Couplings at Colliders*, Ph.D. thesis, Bhubaneswar, Inst. Phys., 2023. [2409.01264](#).

- [39] G. 't Hooft and M. Veltman, *Regularization and renormalization of gauge fields*, *Nuclear Physics B* **44** (1972) 189.
- [40] R. Kleiss, W. J. Stirling and S. D. Ellis, *A New Monte Carlo Treatment of Multiparticle Phase Space at High-energies*, *Comput. Phys. Commun.* **40** (1986) 359.
- [41] S. Veseli, *Multidimensional integration in a heterogeneous network environment*, *Comput. Phys. Commun.* **108** (1998) 9 [[physics/9710017](#)].
- [42] G. Lepage, *A New Algorithm for Adaptive Multidimensional Integration*, *J. Comput. Phys.* **27** (1978) 192.
- [43] A. Geist, A. Beguelin, J. Dongarra, W. Jiang, R. Manček and V. S. Sunderam, *PVM: A Users' Guide and Tutorial for Network Parallel Computing*. The MIT Press, 11, 1994, [10.7551/mitpress/5712.001.0001](#).
- [44] S. Dittmaier, *Separation of soft and collinear singularities from one loop N point integrals*, *Nucl. Phys. B* **675** (2003) 447 [[hep-ph/0308246](#)].
- [45] S. Catani and M. H. Seymour, *A General algorithm for calculating jet cross-sections in NLO QCD*, *Nucl. Phys. B* **485** (1997) 291 [[hep-ph/9605323](#)].
- [46] M. Cacciari, G. P. Salam and G. Soyez, *FastJet User Manual*, *Eur. Phys. J. C* **72** (2012) 1896 [[1111.6097](#)].
- [47] M. Cacciari and G. P. Salam, *Dispelling the N^3 myth for the k_t jet-finder*, *Phys. Lett. B* **641** (2006) 57 [[hep-ph/0512210](#)].
- [48] PARTICLE DATA GROUP collaboration, S. Navas et al., *Review of particle physics*, *Phys. Rev. D* **110** (2024) 030001.
- [49] A. Buckley, J. Ferrando, S. Lloyd, K. Nordström, B. Page, M. Rüfenacht et al., *LHAPDF6: parton density access in the LHC precision era*, *Eur. Phys. J. C* **75** (2015) 132 [[1412.7420](#)].
- [50] M. Guzzi, T. J. Hobbs, K. Xie, J. Huston, P. Nadolsky and C. P. Yuan, *The persistent nonperturbative charm enigma*, *Phys. Lett. B* **843** (2023) 137975 [[2211.01387](#)].
- [51] T.-J. Hou et al., *New CTEQ global analysis of quantum chromodynamics with high-precision data from the LHC*, *Phys. Rev. D* **103** (2021) 014013 [[1912.10053](#)].
- [52] NNPDF collaboration, R. D. Ball et al., *The path to proton structure at 1% accuracy*, *Eur. Phys. J. C* **82** (2022) 428 [[2109.02653](#)].